Stirring across the Antarctic Circumpolar Current's Southern Boundary at the Greenwich Meridian, Weddell Sea

Ria Oelerich[1], Karen J. Heywood[1], Gillian M. Damerell[1], Marcel du Plessis[2], Louise C. Biddle[2], and Sebastiaan Swart[2,3]

[1]Centre for Ocean and Atmospheric Sciences, School of Environmental Sciences, University of East Anglia, Norwich, NR4 7TJ, United Kingdom
[2]Department of Marine Sciences, University of Gothenburg, Gothenburg, Sweden
[3]Department of Oceanography, University of Cape Town, Rondebosch, South Africa

Correspondence: Ria Oelerich (riaoelerich@gmail.com)

Abstract. At the Southern Boundary of the Antarctic Circumpolar Current (ACC), relatively warm ACC waters encounter the colder waters surrounding Antarctica. Strong density gradients across the Southern Boundary indicate the presence of a frontal jet and are thought to modulate the southward heat transport across the front. In this study, the Southern Boundary in the Weddell Sea sector at the Greenwich Meridian is surveyed for the first time in high resolution over an entire austral summer with underwater gliders transecting the front on 5 occasions. The 5 transects show that the frontal structure (i.e., hydrography, velocities and lateral density gradients) varies temporally. The results demonstrate significant, quite rapid (a few weeks) variability of the Southern Boundary and its frontal jet in location, strength and width. A mesoscale cold-core eddy is identified to disrupt the Southern Boundary's frontal structure and strengthen lateral density gradients across the front. The front's barrier properties are assessed using mixing length scales and potential vorticity to establish the cross-frontal exchange of properties between the Southern Boundary and the Weddell Gyre. The results show that stronger lateral density gradients caused by the mesoscale eddy strengthen the barrier-like properties of the front through reduced mixing length scales and pronounced gradients of potential vorticity. In contrast, the barrier-like properties of the Southern Boundary are reduced when no mesoscale eddy is influencing the density gradients across the front. Using altimetry, we further demonstrate that the barrier properties over the past decade have strengthened as a result of increased meridional gradients of absolute dynamic topography and increased frontal jet speeds in comparison to previous decades. Our results emphasize that locally and rapidly changing barrier properties of the Southern Boundary are important to quantify the cross-frontal exchange, which is particularly relevant in regions where the Southern Boundary is located near the Antarctic shelf break (e.g. in the West Antarctic Sector).

1 Introduction

The Southern Ocean hosts one of the largest current systems on earth, the Antarctic Circumpolar Current (ACC). The eastward flow of the ACC circulates the Southern Ocean's major source of heat, Circumpolar Deep Water (CDW), and is characterized by strongly tilted isopycnals shoaling poleward (Orsi et al., 1995). Traditionally, the ACC is described with the three major deep reaching fronts representing boundaries between zones with distinct water mass properties. The seasonal and interannual

variability of transport, extent and location of these fronts have been studied extensively over past decades using water mass properties (e.g., Orsi et al., 1995; Kim and Orsi, 2014), fixed sea surface height (SSH) contours, gradients of SSH and mean

25 transport positions (e.g., Sokolov and Rintoul, 2007, 2009a, b; Billany et al., 2010; Gille, 2014; Gille et al., 2016). Enhanced density gradients across the fronts support strong oceanic jets that form the main contribution to the ACC transport and act as barriers to cross-frontal mixing (Naveira-Garabato et al., 2011; Thompson and Sallée, 2012; Chapman and Sallée, 2017). In some studies, the traditional three-front view of the ACC has been expanded by including the Southern Boundary of the ACC to the south (e.g., Billany et al., 2010). However, its definition is not based on the characteristics of a dynamical front (Talley

30 et al., 2011), but rather as a boundary of water mass properties that separates warm ACC waters from colder water masses further south (Orsi et al., 1995). Therefore, the Southern Boundary is often not considered as part of the ACC (Sokolov and Rintoul, 2007) and its changing properties that can enhance or suppress cross-frontal mixing have not been studied extensively in the past.

35 The focus of this study is the Southern Boundary of the ACC (Fig. 1a), which is traditionally, climatologically and globally defined as the southernmost limit of Upper Circumpolar Deep Water (UCDW, $\Theta > 1.5°C$ and $S > 34.5$, (Orsi et al., 1995)). The proximity of the Southern Boundary to the continental shelf break varies around Antarctica, where its northernmost displacements are located in areas of cyclonic gyres with clockwise surface circulation in the Weddell and Ross Seas. Specifically in areas where the Southern Boundary is located close to the continental shelf, such as in the West Antarctic Sector, it is

40 considered to play an important role in processes that can aid or oppose the influx of warm waters onto the continental shelf (e.g., Dinniman and Klinck, 2004; Jenkins and Jacobs, 2008; Martinson and McKee, 2012). The Southern Boundary and its associated frontal jet further represent the southernmost boundary to mixing (e.g., Naveira-Garabato et al., 2011; Thompson and Sallée, 2012; Chapman and Sallée, 2017; Chapman et al., 2020) and mark the barrier between the northern limit of sea ice formation and the ACC. Thus, whether mixing across the Southern Boundary in summer influences the sea ice formation in

45 the following winter is an important question addressed in this study.

Previous studies have shown that the mean positions of the major ACC fronts have not shifted southward in response to southward migrating, intensifying westerly winds due to recent climate change (e.g., Chapman et al., 2020; Gille, 2014; Shao et al., 2015; Gille et al., 2016). However, analyzed in situ observations, historical reconstructions of ocean conditions, ensemble

50 of coupled climate model simulations and idealized experiments have shown that the ACC's core eastward flow (at 52°S) has accelerated over the past decade (Shi et al., 2021). The acceleration in eastward flow of the ACC was not attributed to changes in wind strength, but rather to intensifying meridional density gradients in response to upper ocean warming. Nonetheless, satellite altimetry and eddy resolving models suggested an intensifying eddy field within the ACC over the past decade in response to the long-term increase in westerly winds (e.g., Meredith and Hogg, 2006; Hogg et al., 2015; Patara et al., 2016).

55 Studies have shown that mesoscale eddies across the ACC fronts sharpen density gradients and thus strengthen the frontal jets (Williams et al., 2007; Hughes and Ash, 2001), which in turn act to suppress the mixing across the ACC fronts and greatly reduce the meridional exchange of properties, such as heat and carbon (Naveira-Garabato et al., 2011). As a consequence,

regions where the ACC fronts have weaker frontal jets, such as downstream of large bathymetric features, are characterized by less suppressed mixing across fronts and thus elevated meridional exchange of properties (e.g., Naveira-Garabato et al., 2011;

60 Thompson and Sallée, 2012). The majority of studies almost entirely focused on the mean positions, transports and barrier properties of the major ACC fronts, whereas processes and dynamics affecting the frontal structure and the frontal jet of the Southern Boundary and meridional exchange of properties across it are poorly understood.

In this study, the Southern Boundary's frontal characteristics, barrier/blender properties and short-term variability in the north-

65 ern Weddell Sea are investigated. We specifically highlight the impacts of mesoscale eddies on the frontal structure of the Southern Boundary and test the hypothesis that eddies interacting with the Southern Boundary affect density gradients, frontal jet intensity, mixing length scales and mixing across the Southern Boundary. For our analysis we use repeat glider transects crossing the Southern Boundary at the Greenwich Meridian (Fig. 1b) and satellite altimetry to: (i) describe the Southern Boundary's frontal structure and frontal jet intensity, (ii) identify the location, rotational direction and dynamics of mesoscale

70 eddies interacting with the Southern Boundary and (iii) establish how eddies impact the Southern Boundary's barrier/blender properties. We further investigate changes of the Southern Boundary's location and frontal jet intensity using AVISO satellite altimetry from 1993 to 2020 and discuss the potential implications for the barrier/blender properties of the front as well as impacts on sea ice extent. This study is organized as follows: section 2 introduces the Southern Boundary's frontal structure and its variability using the five glider transects. Section 3 describes and quantifies the effects of a mesoscale eddy on the

75 frontal structure using two glider transects (transects A and C, Fig. 1b) . Section 4 evaluates mixing length scales and barrier properties of the Southern Boundary. Section 5 provides the main conclusions and offers suggestions for future work.

2   Frontal Structure of the Southern Boundary

As part of the 'Robotic Observations And Modelling in the Marginal Ice Zone' (ROAM-MIZ, www.roammiz.com) project, two Seagliders (SG537 and SG640) were deployed at the Greenwich Meridian in the northeastern Weddell Sea (SG537: 0.00°W

80 and -55°S, SG640: 0.02°W and -55.01°S) and obtained a total of five repeated crossings of the Southern Boundary (Fig. 1, transects A-E). The average time taken to complete one crossing of the front was 16.6 days (transect A - 6th to 29th Nov (321.85 km); transect B - 12th Nov to 3th Dec (211.90 km), transect C - 29th Nov to 7th Dec (202.13 km); transect D - 7th Dec to 22th Dec (145.56 km) and transect E - 22nd Dec to 6th Jan (152.42 km). All ocean properties use the TEOS10 equation of state (IOC et al., 2010) and therefore temperature will refer to conservative temperature [°C] and salinity will refer to

85 absolute salinity [$\mathrm{g\,kg^{-1}}$] throughout this study. The glider profiles of temperature and salinity (Fig. 2) are vertically-gridded with an interval of 2 m. The gliders also provide an estimate of the currents experienced by the gliders during each dive, the dive average current (DAC). Independently from the DAC, we further provide an estimate of the surface currents by calculating the surface drift of the glider during communication with the satellite at the surface. The glider transects are observed in a cross-front orientation, so that the cross-transect velocities capture the flow associated with the Southern Boundary. The

90 absolute along-stream geostrophic velocities are calculated by referencing the geostrophic shear to the component of the DAC
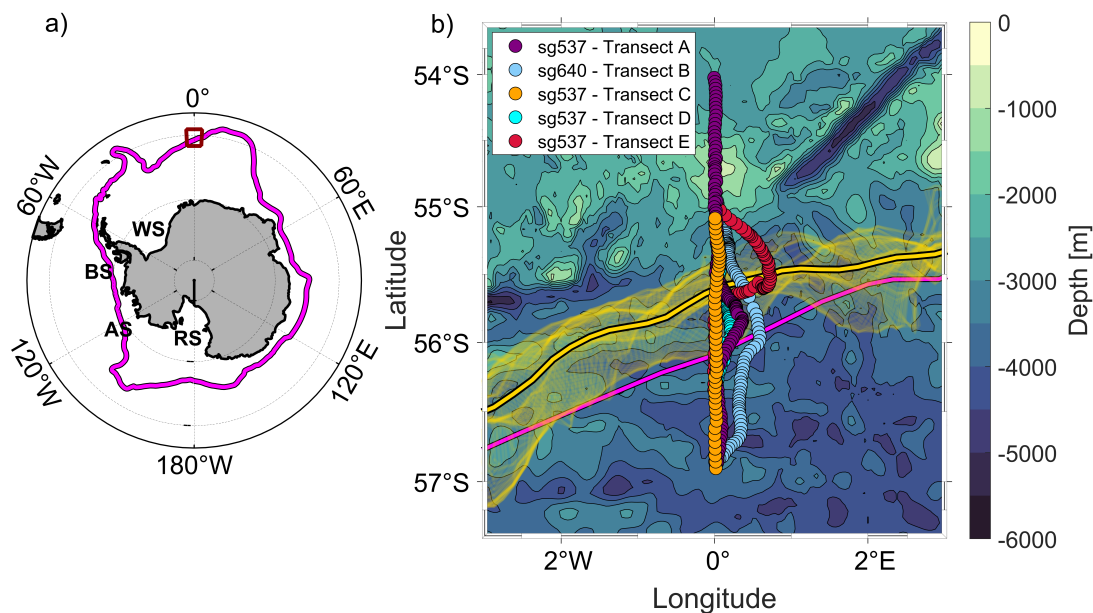
Figure 1. (a) Map of the Southern Ocean with the study region outlined by a red box and the climatological mean location of the Southern Boundary (magenta contour in (a) and (b)) after Orsi et al. (1995)). (b) Five glider transects superimposed on the bathymetry Schaffer et al. (2019). Each colored dot represents the glider's position at the surface following a dive. The -1.16 m contour of absolute dynamic topography from satellite altimetry is shown as a mean over the observational time period (18th October 2019 to 18th February 2020, bold yellow) and daily over the same time period (transparent yellow). The significance of this contour is discussed in the main text of section 2. Key geographic features in (a) are labelled: Ross Sea (RS), Amundsen Sea (AS), Bellingshausen Sea (BS) and Weddell Sea (WS).

perpendicular to the transects. The geostrophic velocities are then horizontally smoothed with a 15 km moving mean filter, which corresponds to the Rossby radius of the region of interest.

This study uses the daily satellite-altimetry-derived global sea level data product (SEALEVEL_GLO_PHY_L4_MY_008_047) provided by the Copernicus Marine Environment Monitoring Service (CMEMS) with a horizontal resolution of 0.25x0.25° (approximately 28 km x 16 km in the study region). It covers the period from 1993 onward (DOI: https://doi.org/10.48670/moi-00148, 2022) incorporating all altimetry-carrying Copernicus missions (Sentinel-6A, Sentinel-3A/B) and other collaborative missions (e.g.: Jason-3, Saral[-DP]/AltiKa, Cryosat-2, OSTM/Jason2, Jason-1, Topex/Poseidon, Envisat, GFO, ERS-1/2, Haiyang-2A/B) (Pujol, 2022). Typically, most recent products are available with a 10-month delay. Absolute dynamic topography (ADT) representing sea surface height above the geoid, sea level anomalies (SLA) and surface geostrophic currents up to December 2020 are used in this study. Note that the SLA provided by the altimetry are relative to the 20-year mean from 1993 to 2012.

All glider transects (Fig. 2 and Fig. 3a,c) display water masses typical of the Southern Boundary at the Greenwich Merid-

105   ian as identified in previous studies (e.g., Orsi et al., 1995). The warming and freshening of the near surface water masses (top 50 m) from transect A to transect E (Fig. 2) are due to solar radiation and sea ice melt respectively as expected during austral spring and summer (October-January observations). The seasonal warming and freshening causes properties, such as temperature and salinity, to deviate from the mean sections more strongly near-surface than at depth (Fig. 3b,d). Antarctic Surface Water (AASW) occupies the top 150-200 m and always lies above Upper Circumpolar Deep Water (UCDW, 200-750 m).

110   UCDW and Lower Circumpolar Deep Water (LCDW, 750-1000 m) occur north of the Southern Boundary. The southernmost limit of UCDW in each glider transect locates the Southern Boundary within 55.55 to 55.82°S (28 km). This highly variable frontal region is identified by greater standard deviations of temperature and salinity (Fig. 3b,d) throughout the water column. The southernmost extent of UCDW (55.82°S) is found in transect D (Fig. 2d,i) and the northernmost extent of the southernmost UCDW (55.55°S) is found in transect C (Fig. 2c,h). The southernmost extent of UCDW found in these transects corresponds

115   well with the location of strong ADT gradients which mark the presence of a frontal jet. The location of strong ADT gradients is in agreement with the work of Billany et al. (2010) who found the Southern Boundary co-located with the southernmost strong ADT gradients across the ACC between 1993 and 2008 within the same region. Moreover, the examination of the daily satellite altimetry over the entire area shown in Fig. 1 reveals that the -1.16 m ADT contour is co-located with strong ADT gradients and strong surface velocities provided by the altimetry that further align with strong velocities indicated by the DAC

120   and surface drift (Fig. 4). Furthermore, the -1.16 m ADT contour is co-located with the southernmost extent of UCDW at the times when the gliders cross the Southern Boundary. This study therefore uses the -1.16 m ADT contour to identify daily locations of the Southern Boundary during the observational period. Note that the identification of the Southern Boundary using the fixed -1.16 m ADT contour is only valid for the observational period (approx. 2 months) and is as previous studies (e.g., Gille, 2014; Gille et al., 2016) demonstrated not appropriate over longer timescales, such as multiple years.

125

    Across the Southern Boundary, most transects (A,B,D,E) demonstrate strong horizontal density gradients (Fig. 2 and Fig. 3) across the Southern Boundary. The 27.73 $\mathrm{kg\,m^{-3}}$ and 27.93 $\mathrm{kg\,m^{-3}}$ isopyncals mark the upper and lower boundary of UCDW and are in general shallowing to the south. The 27.93 $\mathrm{kg\,m^{-3}}$ isopycnal slopes strongly at the location of the Southern Boundary. In addition, in some areas, individual for each transect, the 27.73 $\mathrm{kg\,m^{-3}}$ isopycnal bowls downward. These areas

130   coincide with colder and fresher water mass properties than in the ambient water in the upper 250 m of the water column and are located south of the Southern Boundary. In contrast, transect C demonstrates weaker horizontal density gradients in comparison to the other transects, which is implied by a less steeply sloping 27.93 $\mathrm{kg\,m^{-3}}$ isopycnal. The 27.73 $\mathrm{kg\,m^{-3}}$ isopycnal in transect C also does not bowl downwards and does not show the coincident changes in water mass properties as demonstrated in the other transects.

135

    In summary, we have shown that the location of the Southern Boundary and its frontal structure change on short time scales (approx. 14 days). The following section will focus on transects A and C to identify the processes that influence the frontal structure and specifically modify the horizontal density gradients across the front.
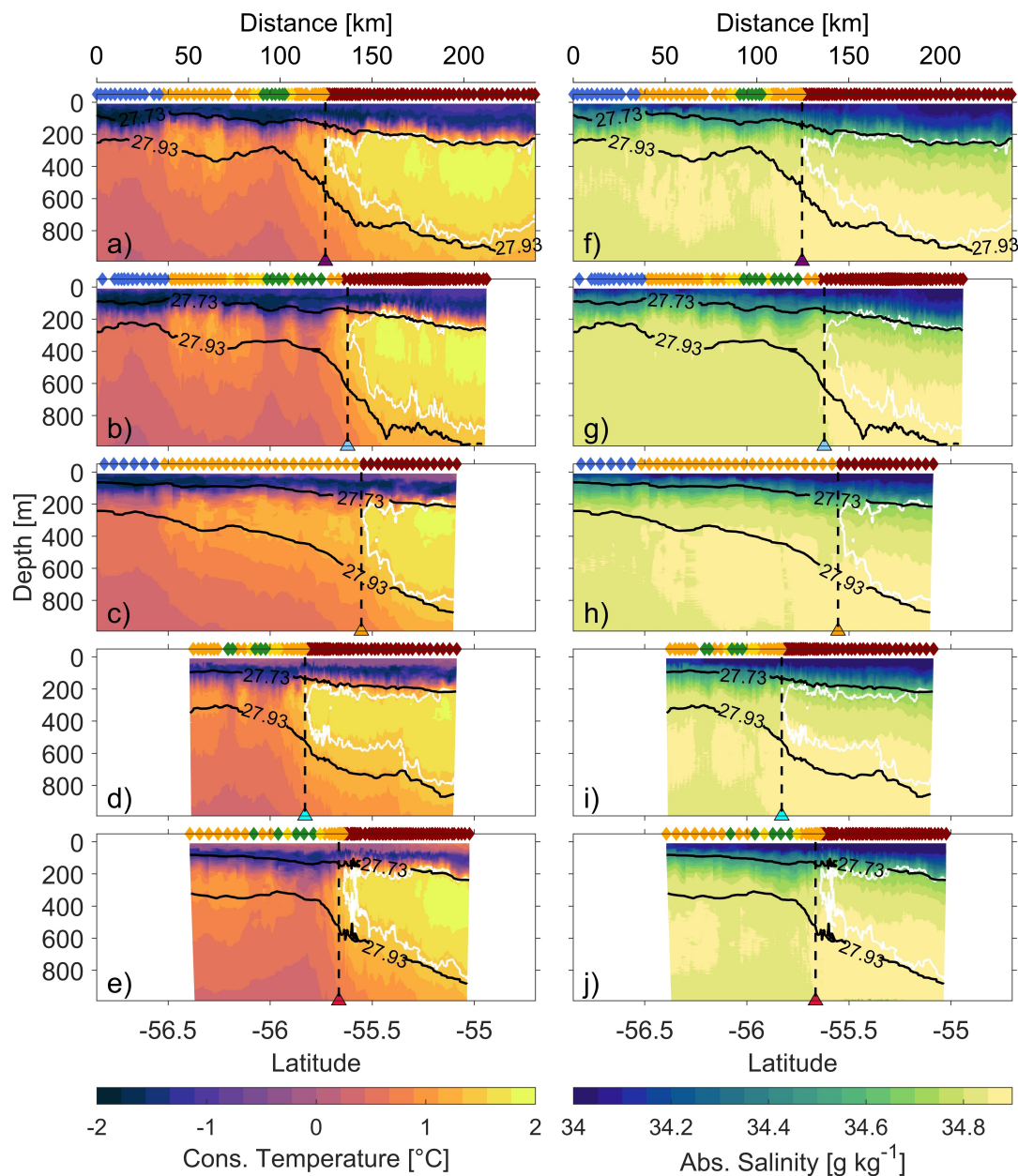
Figure 2. Hydrography of glider transects A-E showing conservative temperature (left column, panels a-e) and absolute salinity (right column, panels f-j) for each transect. Potential density contours of 27.73 kg m^{-3} and 27.93 kg m^{-3} are shown in black. The 1.5°C isotherm is shown with white contours. The triangles at the bottom of each panel, and the black dashed line extending upwards from each triangle, indicate the location of the Southern Boundary defined as the southernmost extent of UCDW (Orsi et al., 1995). The triangles are colored for each individual transect as in Fig. 1, and the same transect color coding is used in Fig. 3. The colors at the top of each panel represent our classification into areas north of the Southern Boundary (red), within a transition zone (orange), within the core of an eddy (green) and on the outer edges of an eddy (yellow), and south of the Southern Boundary (blue). This colour coding is discussed in section 3.
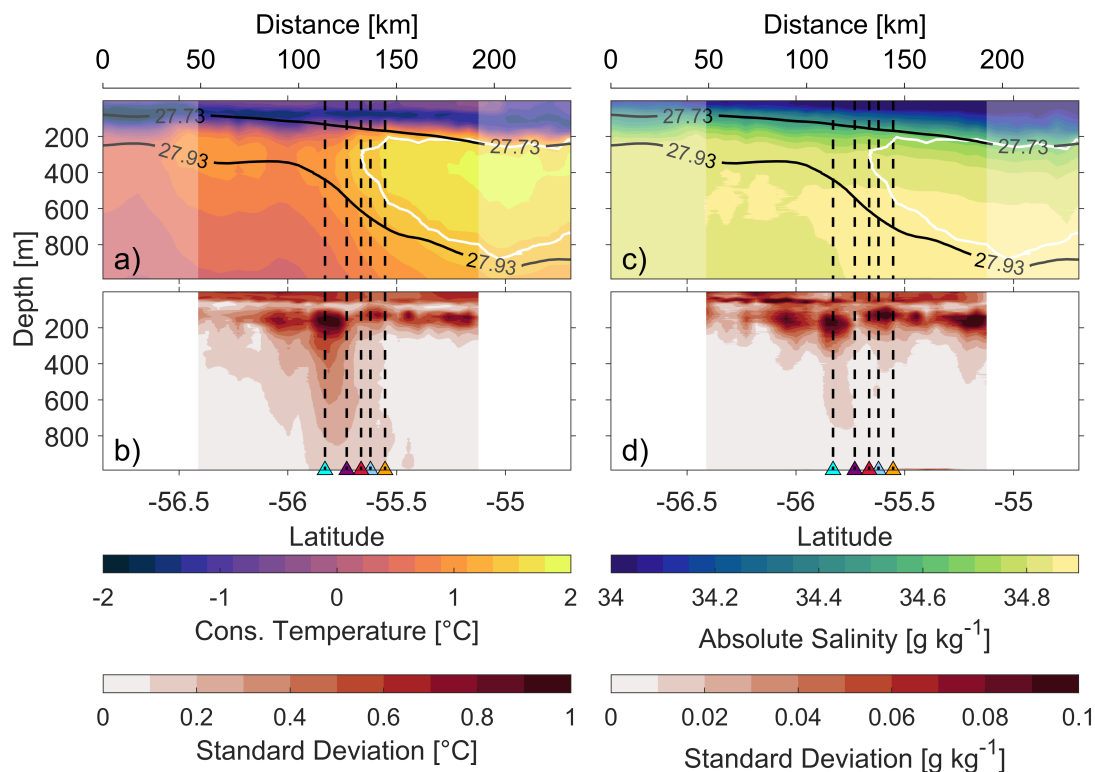
Figure 3. Mean (a,c) and standard deviation (b,d) of all glider transects A-E for (a,b) conservative temperature and (c,d) absolute salinity. The colored triangles at the bottom of panels (b,d), and black dashed lines extending upwards from them are as in Fig. 2. Data from each transect are binned to the same 5 km horizontal grid and then averaged (mean) for all transects. Partially shaded areas on (a,c) indicate areas that do not have data from all transects. Mean isopycnals 27.73 kg m^{-3} and 27.93 kg m^{-3} are shown in black. The white contour indicates the mean 1.5 °C contour.

3 Effects of Mesoscale Eddies on Frontal Structure and Frontal Jet

140   In this study, mesoscale eddies in close proximity to the Southern Boundary (between 54.88°S and 56.63°S) are identified using SLA as introduced in section 2. The specific contours of SLA (0.06, 0.07 and 0.08 m) are chosen to identify mesoscale eddies influencing the frontal structure of the Southern Boundary (Fig. 4). For transect A, the SLA contours (Fig. 4a) reveal a mesoscale eddy (approx. 40 km wide) located to the south of the Southern Boundary at the Greenwich Meridian. In transect A, the glider captures the eddy's core and thus provides information on its rotational direction as well as its water mass properties.

145   Surface current velocities from the altimery, DAC and surface drift from the glider (Fig. 4a) provide evidence for a clockwise-rotating eddy with eastward velocities at its northern edge (55.8°S) and westward velocities at its southern edge (56.2°S). Due to its clockwise rotation, it is implied that the identified eddy is a cold-core eddy. Within a matter of days, the clockwise eddy is

advected to the east with the ACC and is thus not captured again in transect C. As a result, neither sea surface slopes nor DAC nor surface drift from the glider (Fig. 4b) indicate a clockwise rotation. Thus, transect C contains information on the Southern Boundary's frontal structure without an eddy influencing it.

The temperature maximum for each vertical profile of transects A and C (Figs. 4 and 5) displays higher temperatures ($\Theta > 1.8°C$) north and lower temperatures ($\Theta < 0.65°C$) south of the Southern Boundary, thus demonstrating a high to low temperature gradient from north to south in both transects. The main differences between transect A and C in the temperature maximum occur in the transition zone between the warm regime in the north and the cold regime in the south. This is also the region where the clockwise eddy, captured in transect A, is located. Within the transition region, the temperature maximum in transect A demonstrates significantly lower temperatures (0.65-0.8°C at 56°S) than in transect C (Fig. 5), which provides further evidence that the captured eddy in transect A is a cold-core eddy.

North of the Southern Boundary, Θ/S profiles (Figs. 6 and 7) converge towards similar temperatures and salinities ($\Theta > 1.5°C$ and S>34.7) at the base of the thermocline (230 m), which represents UCDW. LCDW is identified below the UCDW layer with slightly lower temperatures ($\Theta \approx 0.6°C$) and similar salinities (S>34.7). In the temperature transition zone, lower temperatures between 0.2-1.2°C indicate the presence of moderately to heavily modified CDW (mCDW), which is representative of the temperature transition zone in both transects. The clockwise eddy identified in transect A (Fig. 6 a,d,e) presents properties similar to the cold regime but with slightly higher temperatures (about 0.4 to 0.6°C higher) below the thermocline and slightly reduced salinities above the thermocline. The similar water mass properties of the eddy and the cold regime suggest that the eddy originated south of the Southern Boundary.

Geostrophic velocities referenced to the DAC (Fig. 8) reveal the frontal jet associated with strong density gradients. Transect A has the most intense jet with an eastward core velocity of up to 80 $\mathrm{cm\,s^{-1}}$ and a meridional extent of about 50 km. In contrast, the frontal jet associated with smaller density gradients is weaker and broader in transect C with an eastward core velocity of up to 60 $\mathrm{cm\,s^{-1}}$ and a meridional extent of about 80 km. The southern edge of the frontal jet is located between 55.5-56°S in both transects and is consistent with the Southern Boundary's location indicated by the southernmost limit of UCDW (Fig. 2) and the gradient of ADT (Fig. 8a,c). Westward velocities south of the Southern Boundary at a depth of 80-400 m between 56-56.5°S in transect A are consistent with the location and cyclonic rotation of the eddy (Fig. 4a) and indicate the eddy's southern edge. Both transects (Fig. 8a,b) show another eastward flow further south (56.25-56.75°S) with velocities of up to 30 $\mathrm{cm\,s^{-1}}$, which marks the boundary between the transition zone and the cold regime south of the Southern Boundary.

The temperature of the temperature maximum for each transect is used to divide each transect into segments (Fig. 5). We introduce a color-coding scheme to show whether a vertical profile is located to the north or south of the Southern Boundary, within the temperature transition zone or within the cold-core eddy. The color-coded segments are used in Figs. 2, 5, 6, 7, 8, 9 and 10. Each transect is segmented by the following criteria:

Table 1. Segmentation values based on the temperature of the temperature maximum for each vertical profile across each transect. The color-coding scheme introduced in Fig. 5 is based on these values.

Segments	$\Theta_{\max}$ [°C]
North of the Southern Boundary	> 1.5
Temperature Transition Zone	0.95-1.5
Outer Eddy	0.8-0.95
Eddy Core	0.65-0.8
South of the Southern Boundary	< 0.65

In summary, we have shown that a clockwise, cold-core eddy located south of the Southern Boundary influences the frontal structure and strengthens the density gradients across the front and intensifies its frontal jet. Additionally, we have demonstrated that density gradients and the frontal jet are weaker across the Southern Boundary after the eddy has been advected eastward. Furthermore, the characterization of different regimes across the Southern Boundary region using the temperature maximum for each vertical profile reveals specific water mass properties for each regime. We further established, based on the similar water mass properties of the cold-core eddy and the cold regime, that the eddy originated south of the Southern Boundary. In the following section, we address how the changes in the frontal structure of the Southern Boundary impact its barrier/blender properties.

4 Effects of Mesoscale Eddies on Mixing Length Scales

Ferrari and Nikurashin (2010) demonstrated that strong mean flows, such as those found within the ACC fronts, can suppress lateral mixing. Naveira-Garabato et al. (2011) further quantified this effect by estimating mixing length scales (MLS) across the three major fronts of the ACC using hydrographic sections with a mesoscale resolution (approx. 50 km station separation). Naveira-Garabato et al. (2011) found that the eddy diffusivities are typically suppressed across the ACC's frontal jets, primarily as a result of reduced mixing lengths. Here we calculate MLS from the highly-resolved transects A and C to assess whether the passage of an eddy across the Greenwich Meridian affects the ability of water to mix across the Southern Boundary.

First, temperature is linearly interpolated onto a potential density grid with an interval of 0.02 kg m^{-3} in the vertical, as used by Naveira-Garabato et al. (2011), and 5 km in the horizontal. Subsequently, the temperature field is spatially smoothed with a 30 km (twice the Rossby Radius) x 0.08 kg m^{-3} moving median filter to filter out small scale effects and approximate a large-scale temperature field, Θ_m, and a large-scale gradient along potential density surfaces, $\nabla_\rho \Theta_m$. Θ_{rms} is a measure of the temperature fluctuations calculated by producing the root mean square of the difference between the spatial-mean temperature field and the temperature fluctuations, Θ'. The mixing length scales, L_{mix}, across the Southern Boundary are then calculated
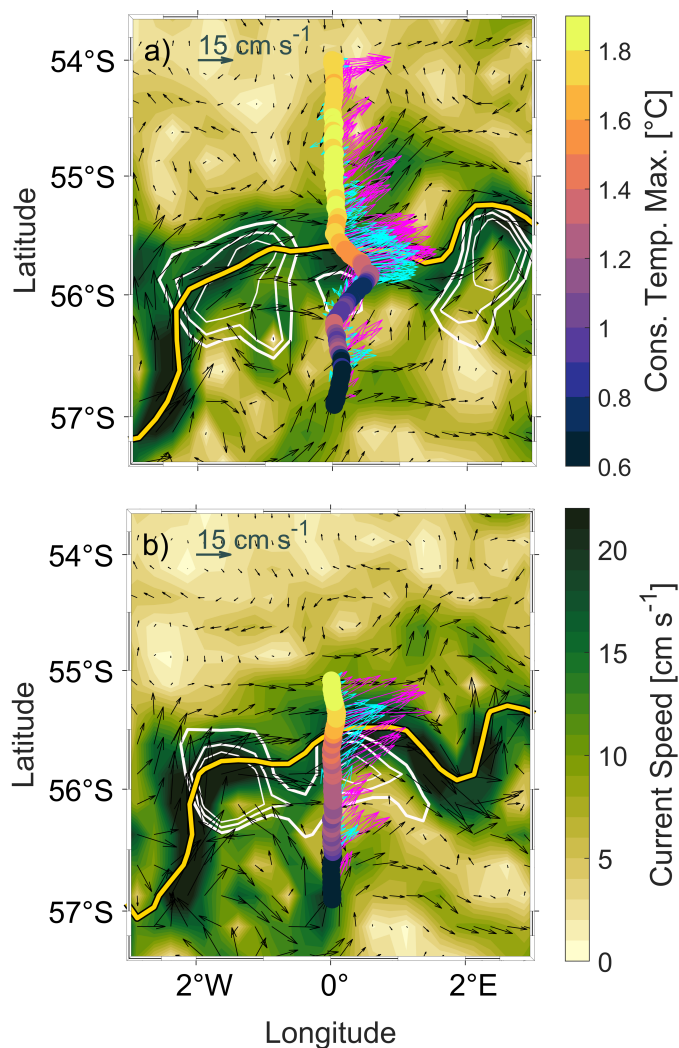
Figure 4. Maps of altimetric sea surface geostrophic velocities (velocity vectors in black and speed in green shading) during the glider crossings of the Southern Boundary for (a) 18th November 2019 (transect A) and (b) 3rd December 2019 (transect C). Bold yellow contours indicate the -1.16 m ADT contour on the same days. Colored dots show the temperature maximum for each vertical profile along the respective transect. Glider dive average currents (magenta vectors) and glider surface drift speeds (cyan vectors) are superimposed. White contours show sea level anomalies of 0.06, 0.07 and 0.08 m (thin to bold) and indicate the location of clockwise eddies in close proximity to the Southern Boundary.
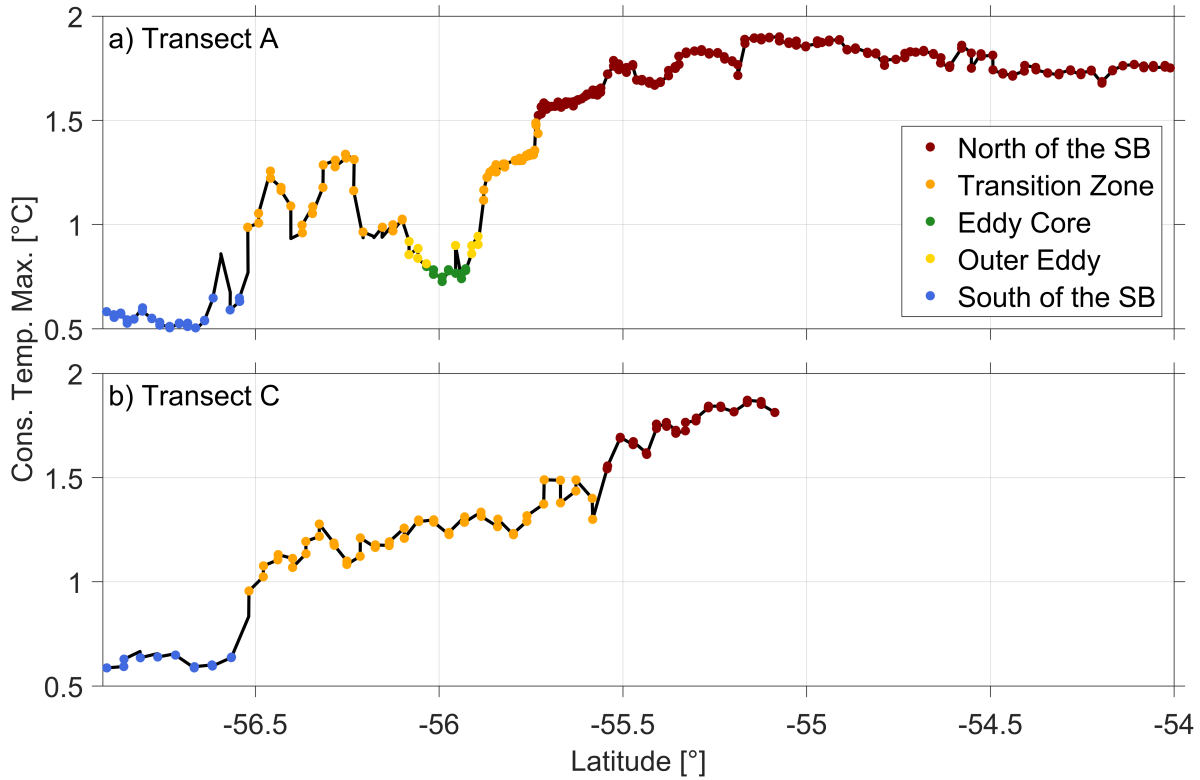
Figure 5. The color-coded temperature maximum for each vertical profile along (a) transect A and (b) transect C. The segmentation values for each regime, on which the color-coding is based, are defined in Table 1 in section 3 .

205 from:

$$L_{mix} = \frac{\Theta_{rms}}{\nabla_\rho \Theta_m}. \tag{1}$$

We further calculate potential vorticity, which is a largely and materially conserved property in the ocean interior that can be used to identify the susceptibility of the flow to instabilities (Haine and Marshall, 1998). The Ertel potential vorticity (PV) can be written as:

210 $$Q = (f\hat{k} + \nabla \times \mathbf{u}) \cdot \nabla b, \tag{2}$$

where f is the Coriolis parameter, g the gravitational acceleration, $\nabla \times \mathbf{u}$ is the relative vorticity, where $\mathbf{u}$ the velocity vector. $b = -g((\rho - \rho_0)/\rho_0)$ is the buoyancy, where ρ is the ocean density and ρ_0 is the reference ocean density. In this study, the glider transects only provide the cross-section (along-stream) velocity component. Therefore the PV has to be simplified to
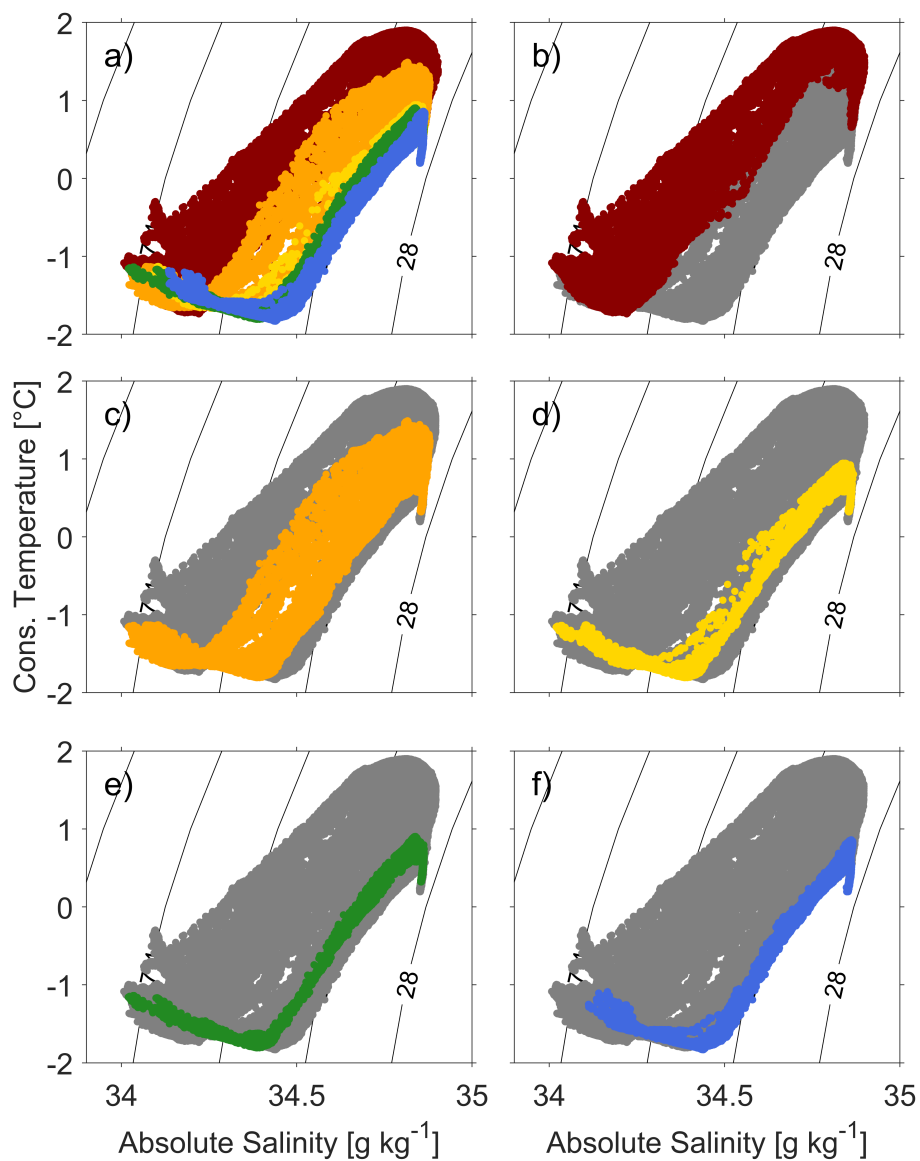
Figure 6. Θ/S diagrams for Transect A with color-coding defined in Table 1 and colors shown in Fig. 5. (a) All profiles of transect A shown with color-coding. (b-f) Grey dots show all profiles in the transect, with colored dots showing the profiles: (b) north of the Southern Boundary, c) in the temperature transition zone, d) in the outer eddy, e) in the eddy core and f) south of the Southern Boundary.
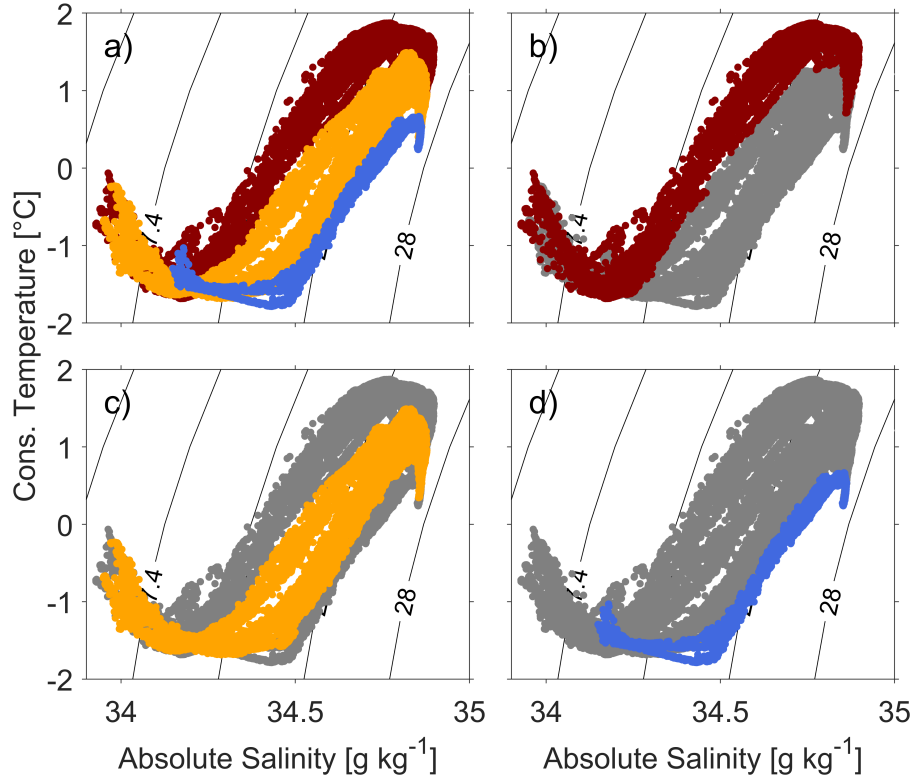
Figure 7. As for Fig. 6 but for transect C.

achieve the observational PV (Azaneu et al., 2017).

$$PV = -\frac{\partial v}{\partial z}\frac{\partial b}{\partial v} + \frac{\partial v}{\partial x}\frac{\partial b}{\partial z} + f\frac{\partial b}{\partial z},$$ (3)

215

where the first and second term correspond to the horizontal and vertical components of the relative vorticity. The third term corresponds to the stretching term which is proportional to the vertical stratification (Azaneu et al., 2017). The observational PV simplification assumes that the along-stream buoyancy gradients are much weaker than the cross-stream buoyancy gradients. The PV is further considered along potential density surfaces with the same vertical and horizontal gridding as for the calculation of L_{mix}.

220

The MLS diagnostics show differences between transect A (Fig. 9) and transect C (Fig. 10). The magnitude of $\nabla_\rho\Theta_m$ across the Southern Boundary is substantially larger in transect A (Fig. 9c) than transect C (Fig. 9c), where maximum $\nabla_\rho\Theta_m$ aligns with the southern edge of the frontal jet (Fig. 8) in both transects. The transects further demonstrate enhanced $\nabla_\rho\Theta_m$ near 56.5°S representing the second, weaker velocity core that marks the boundary between the transition zone and the cold regime further south. The magnitude of Θ_{rms} in both transects (Fig. 9b and Fig. 10b) is largest along the upper boundary of UCDW

225
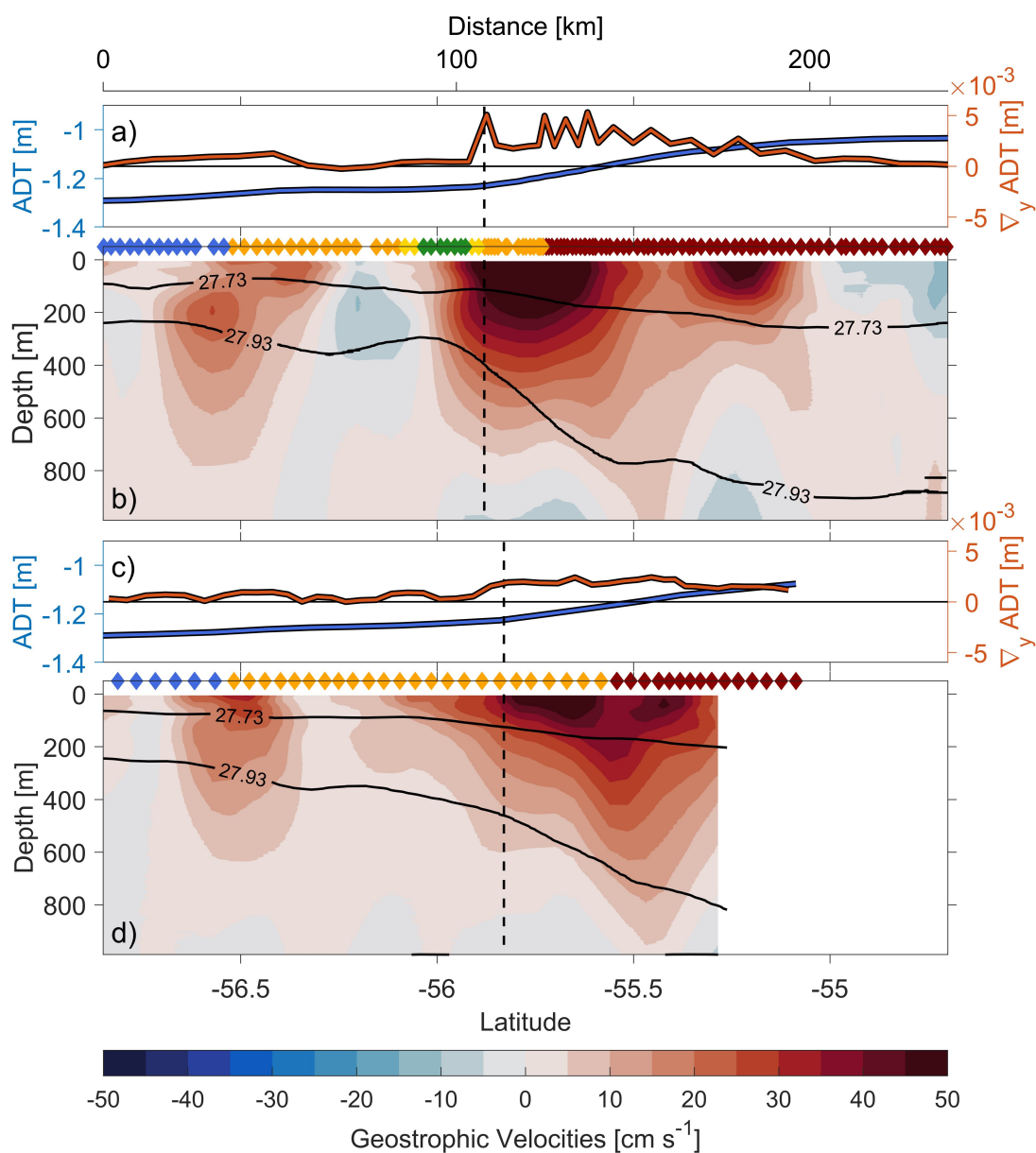
Figure 8. Real-time altimetric ADT and gradients of ADT (∇_yADT) for (a) transect A and (c) transect C. (b,d) Geostrophic velocities perpendicular to the respective glider transects A and C and referenced to the DAC with a horizontal smoothing (moving mean filter) of approx. 15 km (Rossby radius within the region of interest). Positive geostrophic velocities are defined as eastwards (red). Black contours are as in Fig. 2. Color-coding at the top of each panel is defined in Table 1 with colors shown in Fig. 5. The dashed black lines indicate the location of the Southern Boundary based on the southernmost strong ADT gradient.

and mCDW and reflects fluctuations in the transition to denser water masses below and to the south. The resulting L_{mix} for transect A (Fig. 9d) and transect C (Fig. 10d) differ by an order of magnitude across the Southern Boundary. Transect A exhibits near zero L_{mix} distinctly confined between 55.5-56°S within the 27.6 kg m^{-3} and 28 kg m^{-3} isopycnals. The region

230 of low L_{mix} coincides with the region of strongest eastward velocities of the frontal jet and southernmost gradients of ADT (Fig. 8a,b) as well as strongest magnitudes of $\nabla_\rho \Theta_m$ (Fig. 9c). The low magnitude of L_{mix} in transect A is classified as eddy suppressing as values as eddy diffusivities are proportional to L_{mix} ($\kappa = U_e L_{mix} c_e$, where U_e is the eddy velocity scale, and c_e is the eddy mixing efficiency). These results imply that the ability of water to move across the Southern Boundary is suppressed for transect A, which is consistent with all other transects that have strong density gradients across the Southern

235 Boundary (transects B, D and E; not shown). The stronger density gradients (transects A, B, D and E) are associated with eddies passing the Greenwich Meridian south of the Southern Boundary and influencing its frontal structure and frontal jet. In contrast, transect C exhibits increased L_{mix} of up to 20 km across the Southern Boundary, and the region of lower L_{mix} is not as clearly confined to the region between 55.5-56°S as in transect A, which suggests that the ability of water to flow across the Southern Boundary is increased in transect C.

240

In general, PV is largest near the surface and decreases with depth towards zero (Figs. 9e and 10e). Between the 27.5 kg m^{-3} and the 27.7 kg m^{-3} isopycnals in transect A, the PV increases sharply from PV$<< -8 \cdot 10^{-9} s^{-3}$ (south of the Southern Boundary) to PV$\approx -3 \cdot 10^{-9} s^{-3}$ (north of the Southern Boundary). The mesoscale eddy influencing the Southern Boundary leads to larger PV (centered around 56°S) coinciding with the eddy's location determined from the temperature maximum

245 (color-coding). In contrast, the PV in transect C does not increase sharply between the 27.5 kg m^{-3} and the 27.7 kg m^{-3} isopycnals. In transect A, at the 27.8 kg m^{-3} isopycnal, which marks the upper boundary of UCDW (centered within the isopycnals of low L_{mix}), the PV also increases sharply across the front from PV$\approx -2.59 \cdot 10^{-9} s^{-3}$ (south of the Southern Boundary) to PV$\approx -0.8 \cdot 10^{-9} s^{-3}$ (north of the Southern Boundary) in a more pronounced way than in transect C. Similar to the analysis of (Bower et al., 1985) for the Gulf Stream, the gradients in PV across the Southern Boundary indicate enhanced

250 barrier-like properties in transect A compared with transect C. Although the PV gradients and low L_{mix} indicate an impedance to cross-frontal mixing, increasing L_{mix} values near the surface suggest that there is still some exchange taking place between regions north and south of the front.

These results indicate that changes in L_{mix} and differing PV gradients in transects A and C are linked to the mesoscale

255 cold-core eddy influencing the density gradients across the Southern Boundary in transect A. As revealed in section 3, the cold-core eddy passing the Greenwich Meridian interrupts the temperature transition zone, strengthens the density gradients across the Southern Boundary and amplifies the frontal jet in transect A. The suppressed L_{mix} and more pronounced PV gradients imply that the ability of properties such as heat and freshwater to cross the Southern Boundary is dampened. In contrast, after the cold-core eddy has been advected away to the east, we find no interruption of the temperature transition zone, weak-

260 ened density gradients and a broader and weakened frontal jet with increased and less confined L_{mix} and less pronounced PV
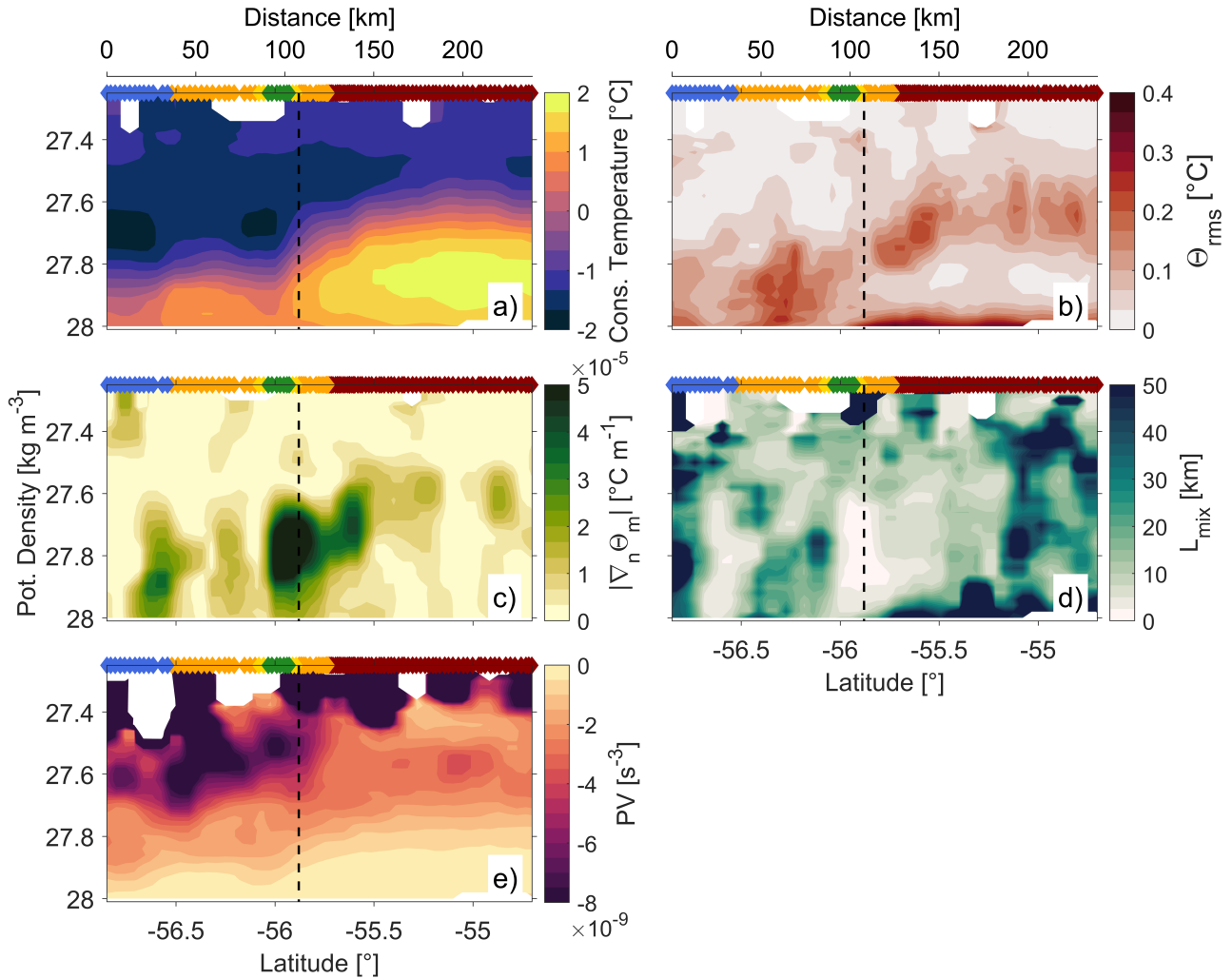
Figure 9. (a) The mean temperature field Θ_m, (b) the measure of the temperature fluctuations Θ_{rms}, (c) the gradient of the mean temperature $\nabla_\rho\Theta_m$ along potential density surfaces, (d) the mixing length scales L_{mix} and (e) the potential vorticity (PV) for transect A. All panels are spatially smoothed by a 30 km x 0.08 kg m^{-3} moving median filter. The dashed black line indicates the location of the Southern Boundary as defined with gradients of ADT as shown in Fig. 8. All subfigures a-e are shown in density space with a vertical gridding of 0.02 kg m^{-3}. The color-coded diamonds at the top of each panel describe the segments along transect A as defined in Table 1

gradients across the front which further suggests the increased ability to exchange water mass properties across the Southern Boundary.
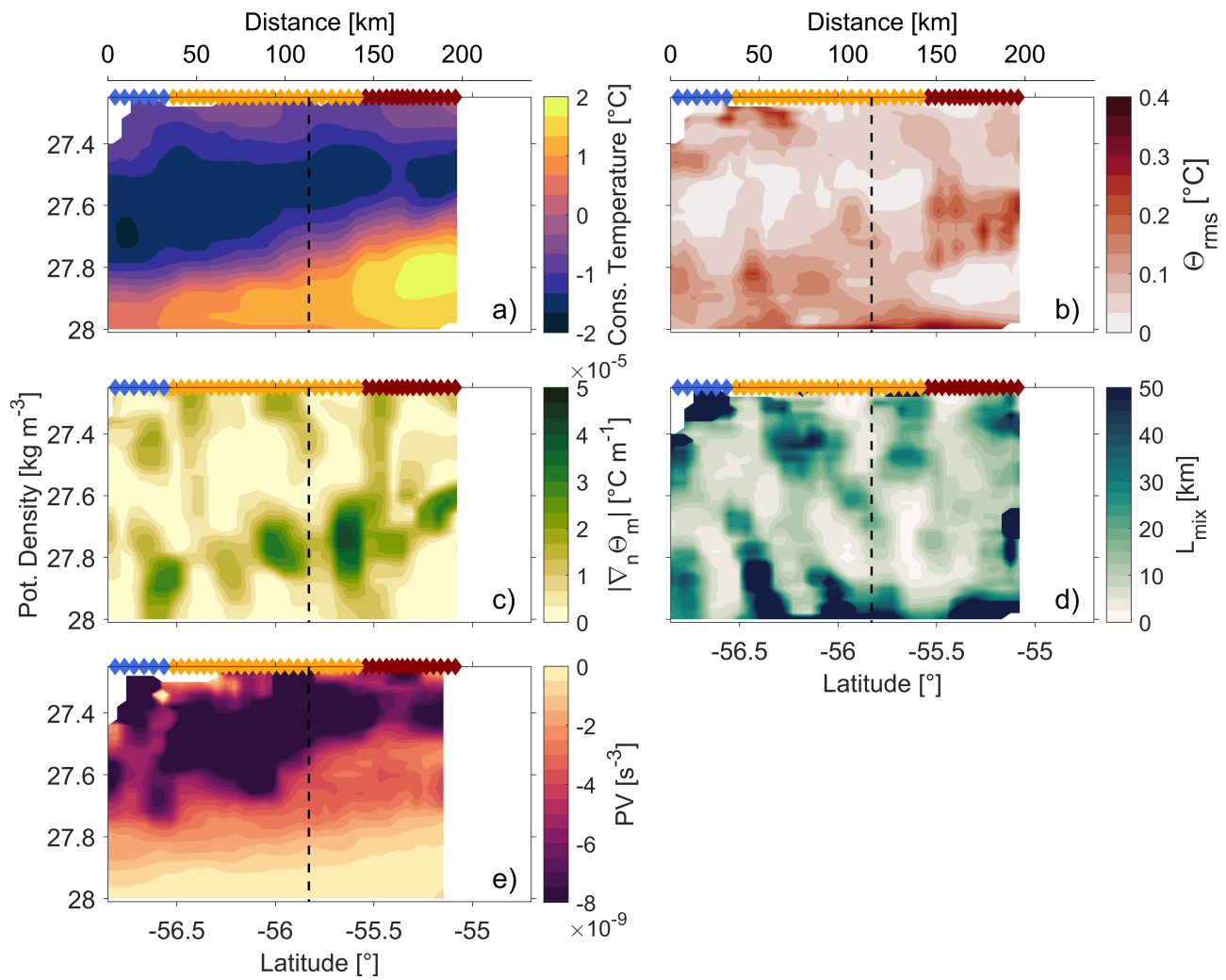
Figure 10. As for Fig. 9 but for transect C.

4.1 Interannual Variability of Barrier Properties

We have shown that the Southern Boundary's barrier properties (as represented by MLS) are related to the magnitude of the
frontal jet. Therefore the strength of the frontal jet, routinely monitored by satellite altimetry, can be used as a proxy to determine the variability of the barrier strength of the Southern Boundary over long time scales (28 years of altimetry data are available). Previous studies have concluded that the use of a fixed ADT contour to define the location of the ACC's fronts is inappropriate over long time scales (such as multiple years), since even if seasonal cycles were removed the long-term warming of ACC waters and associated changes in ADT would not be eliminated (thermal expansion, (Gille, 2014)). Therefore, we estimate the Southern Boundary's location and barrier properties from 1993 to 2020 using surface frontal jet speeds calculated from sea surface slopes (Fig. 11) rather than using specific contours of ADT. The chosen speed contour to highlight enhanced frontal jet speed is 14.5 [$\mathrm{cm\,s^{-1}}$], which is determined from the mean frontal jet speed averaged across the latitude band from 54.87-56.62°S plus twice the standard deviation.

The Southern Boundary's location (determined from the frontal jet) has not migrated south and remains within the 54.87-56.62°S latitude band throughout the 1993-2020 period (Fig. 11). This contrasts with the southward migrating and intensifying westerly winds over the same time period (e.g., Chapman et al., 2020; Gille, 2014; Graham et al., 2012). The average frontal jet speeds across the latitude band (Fig. 11d) indicate that the frontal jet speed has accelerated over the past decade (>14.5 $\mathrm{cm\,s^{-1}}$, 2012-2020). This increase in frontal jet speeds is associated with stronger gradients in ADT across the Southern Boundary (Fig. 11), with an increase in ADT north of the Southern Boundary and no identifiable change in ADT south of the Southern Boundary. These results are consistent with Stewart (2021) and Shi et al. (2021) who demonstrated that the core eastward flow of the ACC has accelerated over the past decade. Stewart (2021) and Shi et al. (2021) further showed that the acceleration in eastward flow is related to the amplification of meridional density gradients in response to upper ocean warming within the ACC, rather than intensifying westerly winds. These results suggest that barrier properties of the Southern Boundary have strengthened over the past decade, associated with strong gradients in PV and density leading to suppressed MLS as shown in section 4. We did not find a significant relationship between the changing barrier properties of the Southern Boundary and the northernmost extent of sea ice concentration (Fig. 11, white contours). In summary, the potential the exchange of properties such as heat and carbon across the Southern Boundary was dampened over the past decade due to the acceleration of the frontal jet. The continuation of upper ocean warming may further increase meridional ADT gradients resulting in an accelerated frontal jet and strengthened barrier properties of the Southern Boundary in the future.

Satellite altimetry observations and eddy resolving models suggest an intensifying eddy field in response to stronger winds (e.g., Meredith and Hogg, 2006; Hogg et al., 2015; Patara et al., 2016). At the Greenwich Meridian we see an increasing number of warm core eddies (Fig. 11b) (and increased EKE, not shown) with increased current speeds south of the Southern Boundary (Fig. 11c) from 2009 onwards. Warm core eddies moving south across the front may thus provide a more dominant
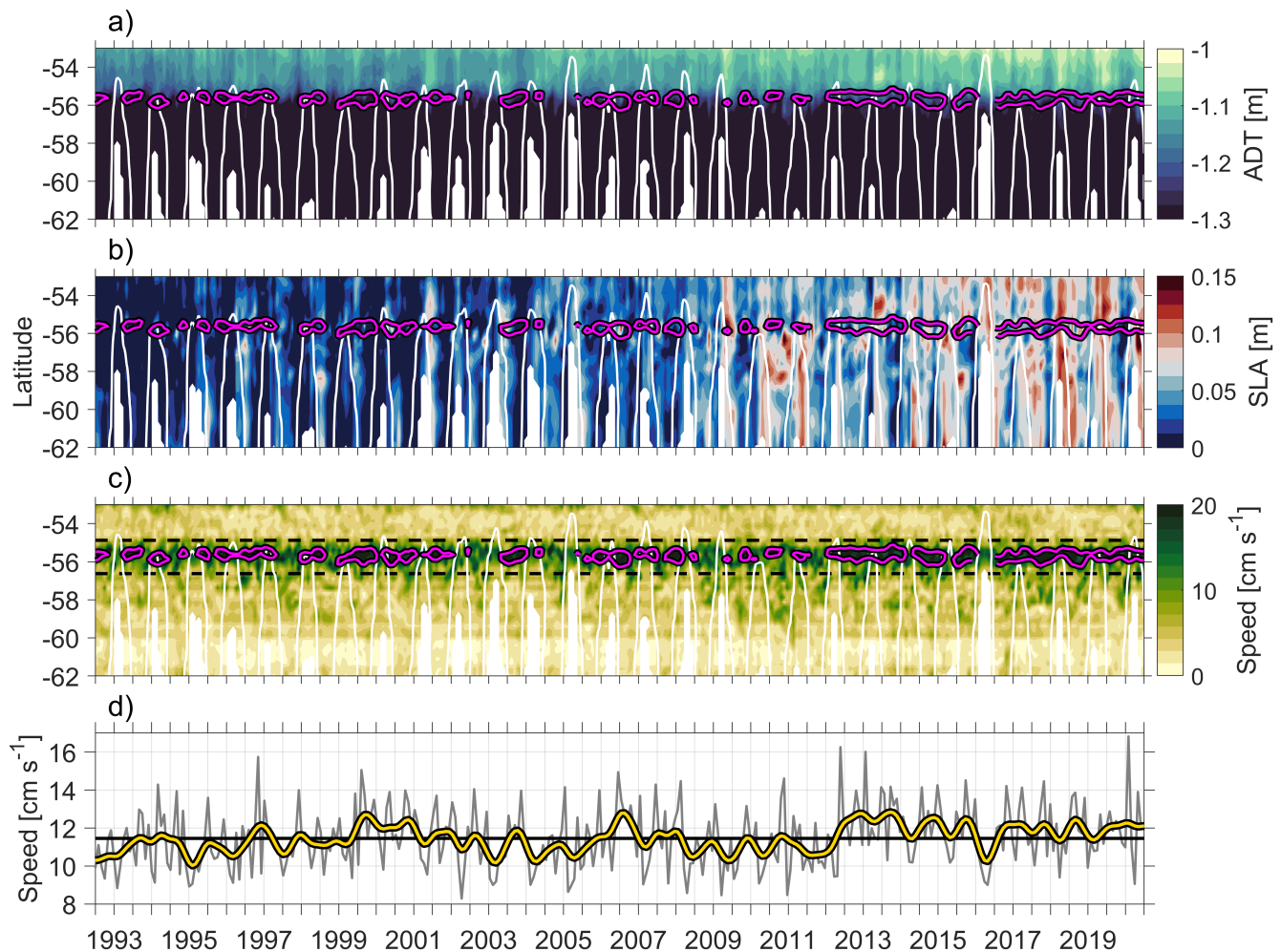
Figure 11. Hovmöller diagrams of a meridional transect at the Greenwich Meridian from altimetry showing (a) ADT, (b) SLA and (c) current speed. In panels (a-c), the white contours indicate the OSTIA sea ice concentration (15%) provided by CMEMS (DOI: https://doi.org/10.48670/moi-00168). Panel (d) displays the averaged frontal jet speed within the 54.87-56.62°S latitude band (dashed black lines in (c)), with the monthly-average frontal jet speeds (grey) and smoothed (12-month moving median filter) frontal jet speeds (yellow). The magenta contours in (a), (b) and (c) highlight periods of enhanced frontal jet speeds (>14.5 cm s^{-1}).

contribution to the transport of properties across the Southern Boundary in the future as barrier properties strengthen through acceleration.

5 Conclusions

In this study we use three months of repeat, high-resolution glider transects over the Antarctic Circumpolar Current's Southern
300 Boundary to assess its variability in location and intensity in terms of lateral gradients and velocities. During the observational
time period, the Southern Boundary was located between 55.5-56°S, where the gradients in ADT and the southernmost limit
of UCDW coincided. The estimated location is consistent with previously estimated locations of the Southern Boundary (e.g.,
Billany et al., 2010). Most glider transects (except transect C) are characterized by strong density gradients across the front
associated with a strong frontal jet ($\approx 80\,\mathrm{cm\,s^{-1}}$), whereas transect C demonstrated weaker density gradients associated with a
305 weaker, broader frontal jet ($\approx 60\,\mathrm{cm\,s^{-1}}$).

The glider transects and SLA revealed that mesoscale cold-core eddies influence the Southern Boundary's frontal structure
by disrupting the temperature transition zone, enforcing stronger density gradients across the front and amplifying the frontal
jet. These findings are consistent with (e.g., Williams et al., 2007) who demonstrated that eddies impact lateral density gradients
310 across the ACC that can accelerate or decelerate the mean flow. We find cold-core eddies are present in all transects that have
a disrupted transition zone and strong density gradients (example transect A). In contrast, we show that the cold-core eddy in
transect A is advected away eastward before transect C is occupied, which then does not cross the cold-core eddy and presents
weaker density gradients and a weaker, broader frontal jet. The highly energetic eddy field within the ACC varies rapidly and
locally around the Antarctic continent and thus more observations are needed to address the impacts of mesoscale eddies on
315 the Southern Boundary's frontal structure in a circumpolar fashion. Future investigations with a focus on regions where the
influences of mesoscale eddies on the Southern Boundary's frontal structure are more or less significant may improve estima-
tions of its barrier properties.

Low L_{mix} and more pronounced PV gradients at the Southern Boundary are found at the upper boundary of UCDW (ex-
320 ample transect A, Fig. 9 d) associated with strong density gradients and an amplified frontal jet. These characteristics suggest
that the exchange of properties across the Southern Boundary is dampened. Thus, it is implied that strengthened barrier prop-
erties are a result of cold-core eddies enforcing stronger density gradients across the Southern Boundary. In contrast, increased
values of L_{mix} of up to 20 km and less pronounced PV gradients across the Southern Boundary (example transect C, Fig.
10 d) are found when no cold-core eddy is observed to influence the Southern Boundary's frontal structure (weaker density
325 gradients, weaker frontal jet). These findings emphasize that locally changing mesoscale structures can significantly impact
the Southern Boundary's barrier properties and thus modulate cross-frontal exchange of properties such as heat and carbon.
The cross-frontal exchange of properties is specifically relevant to regions where the Southern Boundary is located near the
continental shelf break, such as in the West Antarctic Sector, as the amount of heat accessing the continental shelf is modulated
by the front's barrier properties.
330

Additionally, we have shown that the linkage between MLS and the intensity of the frontal jet of the Southern Boundary

is important to establish the Southern Boundary's barrier properties over long time periods (multiple years). Increased ADT gradients across the Southern Boundary, as a result of increased ADT north of the front (Fig. 11a), confirm amplified frontal jet speeds from 2009 onwards. This is consistent with the amplification of the ACC's eastward flow demonstrated by Shi et al.

335 (2021) and Stewart (2021). Based on our results, strengthened density gradients across the Southern Boundary and thus an intensified frontal jet are indicators for dampened cross-frontal exchange and strengthened barrier properties. Thus, we suggest that the poleward heat transfer through mixing across the Southern Boundary at the Greenwich Meridian has likely decreased over the last decade, whereas the intensified eddy field and generation of warm-core eddies that cross the Southern Boundary in response to intensifying westerly winds likely provided an increased contribution to poleward heat transfer. As these processes

340 vary locally and temporarily, our results demonstrate that more investigations of the Southern Boundary's frontal jet intensity and barrier properties are needed to understand and estimate the cross-frontal exchange around the Antarctic continent in more detail.

Data availability. Quality controlled, vertically gridded data from the two Seagliders are available from the following links: SG537, DOI: 10.5281/zenodo.7472263 and SG640, DOI: 10.5281/zenodo.7472428. The altimetry and sea ice concentration data are both provided by the

345 Copernicus Environment Monitoring Service (CMEMS) and are available at: DOI: https://doi.org/10.48670/moi-00148 (altimetry) and DOI: https://doi.org/10.48670/moi-00168 (OSTIA, sea ice concentration).

Author contributions. RO developed the concept for the manuscript; led the writing process; analysed and processed the glider data. The gliders were piloted by RO, KJH, GMD and LBC. KJH, GMD, MdP, SS and LCB provided valuable input and guidance for the development of this study. All authors contributed to the text.

350 *Competing interests.* KJH is a member of the editorial board of Ocean Science

Acknowledgements. The deployment of the glider SG537 and the time of RO, KJH and GMD were supported by funding from the European Research Council (ERC) under the European Union's Horizon 2020 research and innovation programme (COMPASS, Advanced Grant agreement No. 741120).

References

355   Azaneu, M., Heywood, K. J., Queste, B. Y., and Thompson, A. F.: Variability of the Antarctic Slope Current System in the Northwestern Weddell Sea, Journal of Physical Oceanography, 47, 2977–2997, https://doi.org/10.1175/jpo-d-17-0030.1, 2017.

Billany, W., Swart, S., Hermes, J., and Reason, C. J. C.: Variability of the Southern Ocean fronts at the Greenwich Meridian, Journal of Marine Systems, 82, 304–310, https://doi.org/10.1016/j.jmarsys.2010.06.005, 2010.

Bower, A. S., Rossby, H. T., and Lillibridge, J. L.: The Gulf Stream - Barrier or Blender?, Journal of Physical Oceanography, 15, 24–32, 360   https://doi.org/10.1175/1520-0485(1985)015<0024:tgsob>2.0.co;2, 1985.

Chapman, C. C. and Sallée, J.-B.: Isopycnal Mixing Suppression by the Antarctic Circumpolar Current and the Southern Ocean Meridional Overturning Circulation, Journal of Physical Oceanography, 47, 2023–2045, https://doi.org/10.1175/jpo-d-16-0263.1, 2017.

Chapman, C. C., Lea, M.-A., Meyer, A., Sallée, J.-B., and Hindell, M.: Defining Southern Ocean fronts and their influence on biological and physical processes in a changing climate, Nature Climate Change, 10, 209–219, https://doi.org/10.1038/s41558-020-0705-4, 2020.

365   Dinniman, M. S. and Klinck, J. M.: A model study of circulation and cross-shelf exchange on the west Antarctic Peninsula continental shelf, Deep Sea Research Part II: Topical Studies in Oceanography, 51, 2003–2022, https://doi.org/10.1016/j.dsr2.2004.07.030, 2004.

Ferrari, R. and Nikurashin, M.: Suppression of Eddy Diffusivity across Jets in the Southern Ocean, Journal of Physical Oceanography, 40, 1501–1519, https://doi.org/10.1175/2010jpo4278.1, 2010.

Gille, S. T.: Meridional displacement of the Antarctic Circumpolar Current, Philosophical Transactions of the Royal Society A, 372, 1–12, 370   https://doi.org/10.1098/rsta.2013.0273, 2014.

Gille, S. T., McKee, D. C., and Martinson, D. G.: Temporal Changes in the Antarctic Circumpolar Current: Implications for the Antarctic Continental Shelves, The Oceanography Society, 29, 95–106, https://doi.org/10.2307/24862285, 2016.

Graham, R. M., de Boer, A. M., Heywood, K. J., Chapman, M. R., and Stevens, D. P.: Southern Ocean fronts: Controlled by wind or topography?, Journal of Geophysical Research: Oceans, 117, n/a–n/a, https://doi.org/10.1029/2012jc007887, 2012.

375   Haine, T. W. N. and Marshall, J.: Gravitational, Symmetric, and Baroclinic Instability of the Ocean Mixed Layer, Journal of Physical Oceanography, 28, 634–658, https://doi.org/10.1175/1520-0485(1998)028<0634:gsabio>2.0.co;2, 1998.

Hogg, A. M., Meredith, M. P., Chambers, D. P., Abrahamsen, E. P., Hughes, C. W., and Morrison, A. K.: Recent trends in the Southern Ocean eddy field, Journal of Geophysical Research: Oceans, 120, 257–267, https://doi.org/10.1002/2014jc010470, 2015.

Hughes, C. W. and Ash, E. R.: Eddy forcing of the mean flow in the Southern Ocean, Journal of Geophysical Research: Oceans, 106, 380   2713–2722, https://doi.org/10.1029/2000jc900332, 2001.

IOC, SCOR, and IAPSO: The international thermodynamic equation of seawater – 2010: Calculation and use of thermodynamic properties., Intergovernmental Oceanographic Commission, Manuals and Guides No. 56, UNESCO (English), pp. 1–196, https://www.teos-10.org/, 2010.

Jenkins, A. and Jacobs, S.: Circulation and melting beneath George VI Ice Shelf, Antarctica, Journal of Geophysical Research, 113, 385   https://doi.org/10.1029/2007jc004449, 2008.

Kim, Y. S. and Orsi, A. H.: On the Variability of Antarctic Circumpolar Current Fronts Inferred from 1992-2011 Altimetry*, Journal of Physical Oceanography, 44, 3054–3071, https://doi.org/10.1175/jpo-d-13-0217.1, 2014.

Martinson, D. G. and McKee, D. C.: Transport of warm Upper Circumpolar Deep Water onto the western Antarctic Peninsula continental shelf, Ocean Science, 8, 433–442, https://doi.org/10.5194/os-8-433-2012, 2012.

390 Meredith, M. P. and Hogg, A. M.: Circumpolar response of Southern Ocean eddy activity to a change in the Southern Annular Mode, Geophysical Research Letters, 33, https://doi.org/10.1029/2006gl026499, 2006.

Naveira-Garabato, A. C., Ferrari, R., and Polzin, K. L.: Eddy stirring in the Southern Ocean, Journal of Geophysical Research, 116, https://doi.org/10.1029/2010jc006818, 2011.

Orsi, A. H., Whitworth, T., and Nowlin, W. D.: On the meridional extent and fronts of the Antarctic Circumpolar Current, Deep Sea Research
395 I, 42, 641–673, https://doi.org/10.1016/0967-0637(95)00021-W, 1995.

Patara, L., Böning, C. W., and Biastoch, A.: Variability and trends in Southern Ocean eddy activity in 1/12° ocean model simulations, Geophysical Research Letters, 43, 4517–4523, https://doi.org/10.1002/2016gl069026, 2016.

Pujol, M.-I.: PRODUCT USER MANUAL. For Sea Level Altimeter Products. , CMEMS-SL-PUM-008-032-062, pp. 1–42, 2022.

Schaffer, J., Timmermann, R., Arndt, J. E., Rosier, S. H. R., Anker, P. G. D. ., Callard, S. L., Davis, P. E. D., Dorschel, B., Grob, H., Hat-
400 termann, T., Hofstede, C. M., Kanzow, T., Kappelsberger, M., Lloyd, J. M., Ó Cofaigh, C., and Roberts, D. H.: An update to Greenland and Antarctic ice sheet topography, cavity geometry, and global bathymetry (RTopo-2.0.4), https://doi.org/10.1594/PANGAEA.905295, supplement to: Schaffer, Janin; Kanzow, Torsten; von Appen, Wilken-Jon; von Albedyll, Luisa; Arndt, Jan Erik; Roberts, David H (2020): Bathymetry constrains ocean heat supply to Greenland's largest glacier tongue. Nature Geoscience, 13(3), 227-231, https://doi.org/10.1038/s41561-019-0529-x, 2019.

405 Shao, A. E., Gille, S. T., Mecking, S., and Thompson, L.: Properties of the Subantarctic Front and Polar Front from the skewness of sea level anomaly, Journal of Geophysical Research: Oceans, 120, 5179–5193, https://doi.org/10.1002/2015jc010723, 2015.

Shi, J.-R., Talley, L. D., Xie, S.-P., Peng, Q., and Liu, W.: Ocean warming and accelerating Southern Ocean zonal flow, Nature Climate Change, 11, 1090–1097, https://doi.org/10.1038/s41558-021-01212-5, 2021.

Sokolov, S. and Rintoul, S. R.: Multiple Jets of the Antarctic Circumpolar Current South of Australia*, Journal of Physical Oceanography,
410 37, 1394–1412, https://doi.org/10.1175/jpo3111.1, 2007.

Sokolov, S. and Rintoul, S. R.: Circumpolar structure and distribution of the AntarcticCircumpolar Current fronts:1. Mean circumpolar paths, Journal of Geophysical Research, 114, 1–19, https://doi.org/10.1029/2008JC005108, 2009a.

Sokolov, S. and Rintoul, S. R.: Circumpolar structure and distribution of the Antarctic Circumpolar Current fronts: 2. Variability and relationship to sea surface height, Journal of Geophysical Research, 114, 1–15, https://doi.org/10.1029/2008JC005248, 2009b.

415 Stewart, A. L.: Warming spins up the Southern Ocean, Nature Climate Change, 11, 1022–1024, https://doi.org/10.1038/s41558-021-01227-y, 2021.

Talley, L. D., Pickard, G. L., Emery, W. J., and Smith, J. H.: Descriptive Physical Oceanography: an Introduction, Elsevier Ltd., 6 edn., 2011.

Thompson, A. F. and Sallée, J.-B.: Jets and Topography: Jet Transitions and the Impact on Transport in the Antarctic Circumpolar Current, Journal of Physical Oceanography, 42, 956–972, https://doi.org/10.1175/jpo-d-11-0135.1, 2012.

420 Williams, R. G., Wilson, C., and Hughes, C. W.: Ocean and Atmosphere Storm Tracks: The Role of Eddy Vorticity Forcing, Journal of Physical Oceanography, 37, 2267–2289, https://doi.org/10.1175/jpo3120.1, 2007.